Electronic Supplementary Information for

Nanoporous carbons from natural lignin: study of structural-textural properties and application to organic-based supercapacitors

Adriana M. Navarro-Suárez,[a] Javier Carretero-González,*[a] Vladimir Roddatis,[a] Eider Goikolea,[a] Julie Ségalini,[a] Edurne Redondo,[a] Teófilo Rojo*[a] and Roman Mysyk[a]

[a] *CIC energiGUNE, Alava Technology Park, Albert Einstein 48 – ED. CIC, 01510, Miñano, Álava, Spain. Tel: 945297108; E-mail: jcarretero@cicenergigune.com, trojo@cicenergigune.com*

Supplementary results

Energy dispersive X-ray spectroscopy (EDX) analysis

Figure S1 shows the chemical composition of both purified lignin and activated carbons (results for sample 4 are shown in Figure S1(b)) by electron dispersion X-Ray (EDX), analysis carried out in the SEM. Impurities from the Kraft process such as sodium and sulphur still remained in the lignin biopolymer after the extraction; however, they are greatly reduced after chemical activation.

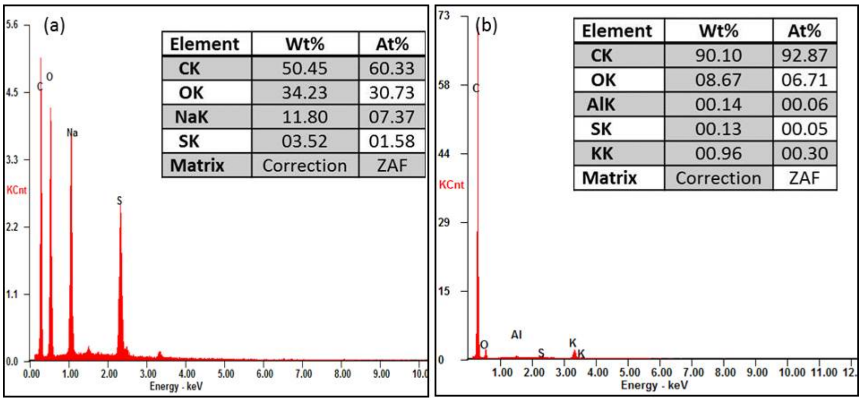

(a)

Element	Wt%	At%
CK	50.45	60.33
OK	34.23	30.73
NaK	11.80	07.37
SK	03.52	01.58
Matrix	Correction	ZAF

(b)

Element	Wt%	At%
CK	90.10	92.87
OK	08.67	06.71
AlK	00.14	00.06
SK	00.13	00.05
KK	00.96	00.30
Matrix	Correction	ZAF

Figure S1. EDX analysis performed at the SEM for (a) the polymer particles of lignin after extraction and (b) the lignin-derived nanoporous carbon.

Textural characterization

Textural properties for the collection of the 8 samples studied in the present work were characterized by nitrogen adsorption/desorption.

The specific surface area (S_{NLDFT}), the micro- ($S_{micro-NLDFT}$) and the mesopore ($S_{meso-NLDFT}$) contribution to the total surface area, average pore size (L_{NLDFT}) and the pore size distribution are obtained after applying the 2D Non Linear Density Functional Theory (NLDFT). The average micropore size (L_{o-DR}), were also determined from the adsorption data using the Dubinin-Radushkevich and Stoeckli equations. A summary of the results extracted from these analyses are shown in Table S1.

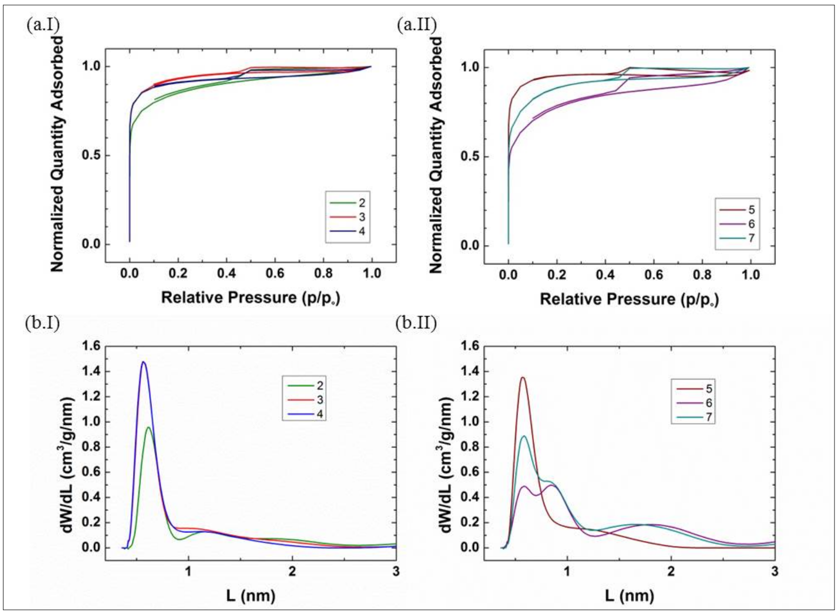

Figure S2. Textural analysis for samples (I) 2, 3 and 4 and (II) 5, 6 and 7. (a) Normalized isotherms of the activated carbon samples and (b) differential pore volume calculated by NLDFT method.

Table S1. Textural properties of the pyrolyzed and activated carbon samples produced from naturally occurring lignin.

Sample	**S_{NLDFT} ($m^2.g^{-1}$)**	**$S_{micro-NLDFT}$ ($m^2.g^{-1}$)**	**$S_{meso-NLDFT}$ ($m^2.g^{-1}$)**	**$L_{microNLDFT}$ (nm)**	**L_{o-DR} (nm)**
0	1	0	1	*	*
1	9	5	4	1.8	*
2	845	797	48	0.9	1.07
3	1280	1259	21	0.8	0.87
4	1272	1254	18	0.76	0.81
5	1236	1234	2	0.79	0.87
6	1406	1311	95	0.96	1.24
7	1262	1196	66	0.98	1.22

Raman Spectroscopy

Acquisition of single Raman spectrum was performed on several particles of the same specimen for the whole series of carbons prepared in this study. At minimum of 10 spectra were taken on different points of the sample particle. Figure S3 shows the typical Raman spectrum corresponding to disordered (blue line) and/or ordered (red line) regions. For all the carbon samples derived from lignin, the low frequency region shows the two characteristic bands for carbonaceous materials; the graphite (G) band between 1570 cm^{-1} and 1600 cm^{-1} and the disorder–induced (D) band between 1330 cm^{-1} and 1360 cm^{-1}. The presence of graphene domains produced the appearance of a weak but well defined band at ~ 2450 cm^{-1} which was due to a non–dispersive overtone mode of an in–plane optical phonon.[i] The G mode has E_{2g} symmetry and involves the in–plane bond–stretching motion of pairs of C sp^2 atoms; while the D peak is a breathing mode with an A_{1g} symmetry involving phonons near the K zone boundary, which only becomes active in the presence of disorder.[ii] At the second-order region appeared the 2D band (2670 – 2760 cm^{-1}), which is due to two phonon with opposite momentum in the highest optical branch near the K point of the Brillouin zone (A'_1 symmetry at K).[iii]

The D and G bands were fitted with 2 symmetric Lorentzian functions;[ii] the I_D/I_G ratio was calculated from the maximum intensities of the simulated peaks and their distribution in a particle is shown in Figures S4 and S5. Crystallite size was calculated from Tuinstra and Koenig (equation S1)[iv] model, where I_D and I_G correspond to the intensities of the simulated peaks D and G respectively, $C_{532\ nm}$ is 4.95[v] and L_a is the cluster diameter.

$$\frac{I_D}{I_G} = \frac{C_\lambda}{L_a} \qquad \textbf{(S1)}$$

For the Raman spectral imaging, a 50X objective lens was used and 10 seconds of exposition time of the laser beam to the sample was taken in areas of at least 600 μm^2. To obtain the Raman images, the sample was moved with a step size of 1 µm and a Raman spectrum was recorded at every point. The spectra were analysed and Raman images were then constructed using the integrated peak intensity by using the Origin Lab® software.

In Figure S4 (and Figure 3) Raman maps are demonstrated coloured according to the ratio of the peaks intensities, showing the distribution of ordered as well as disordered areas. The presence of more ordered areas increases as the KOH/C ratio increases obtaining almost completely organized zones for samples 4, 5, 6 and 7.

The probability distribution of I_D/I_G in a particle in the different samples is shown in Figure S5; the area of each rectangle represents the frequency of points with an I_D/I_G ratio corresponding to each interval and the total area is equal to the number of spectra taken in each sample. Samples 1, 4 and 7 showed almost no deviation from the main peaks and the carbons appeared either disordered (sample 1) or ordered (samples 4 and 7). In samples 2, 3, 5 and 6, the presence of outliers of low frequency is observed which indicates that for these ratios the morphology of the carbon is more heterogeneous, even though the majority of the structure is disorganized (samples 2 and 3) or organized (samples 5 and 6).

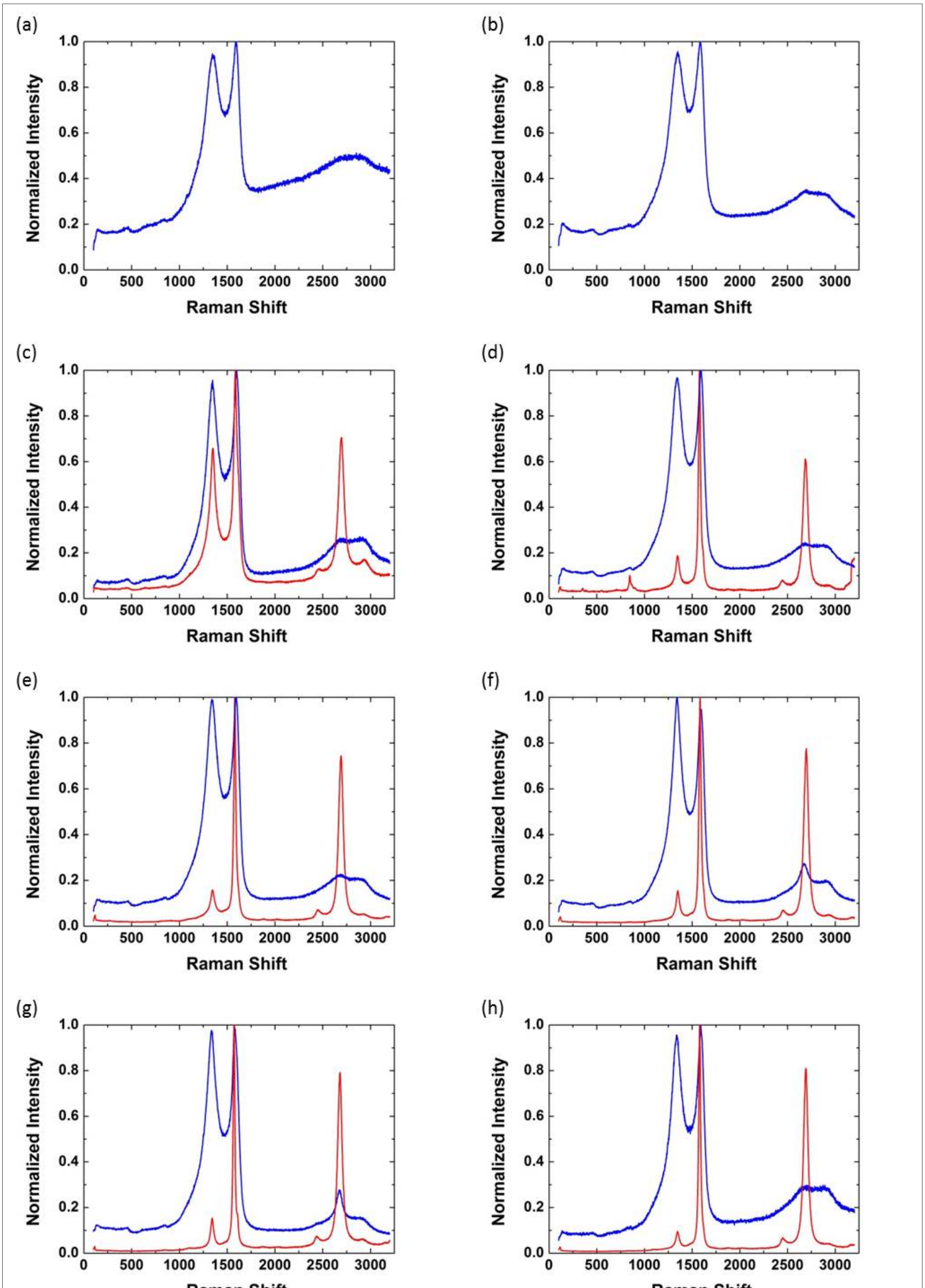

Figure S3. Normalized Raman spectra of samples (a) 0, (b) 1, (c) 2, (d) 3, (e) 4, (f) 5, (g) 6 and (h) 7; depicting the two different spectra observed in different particles.

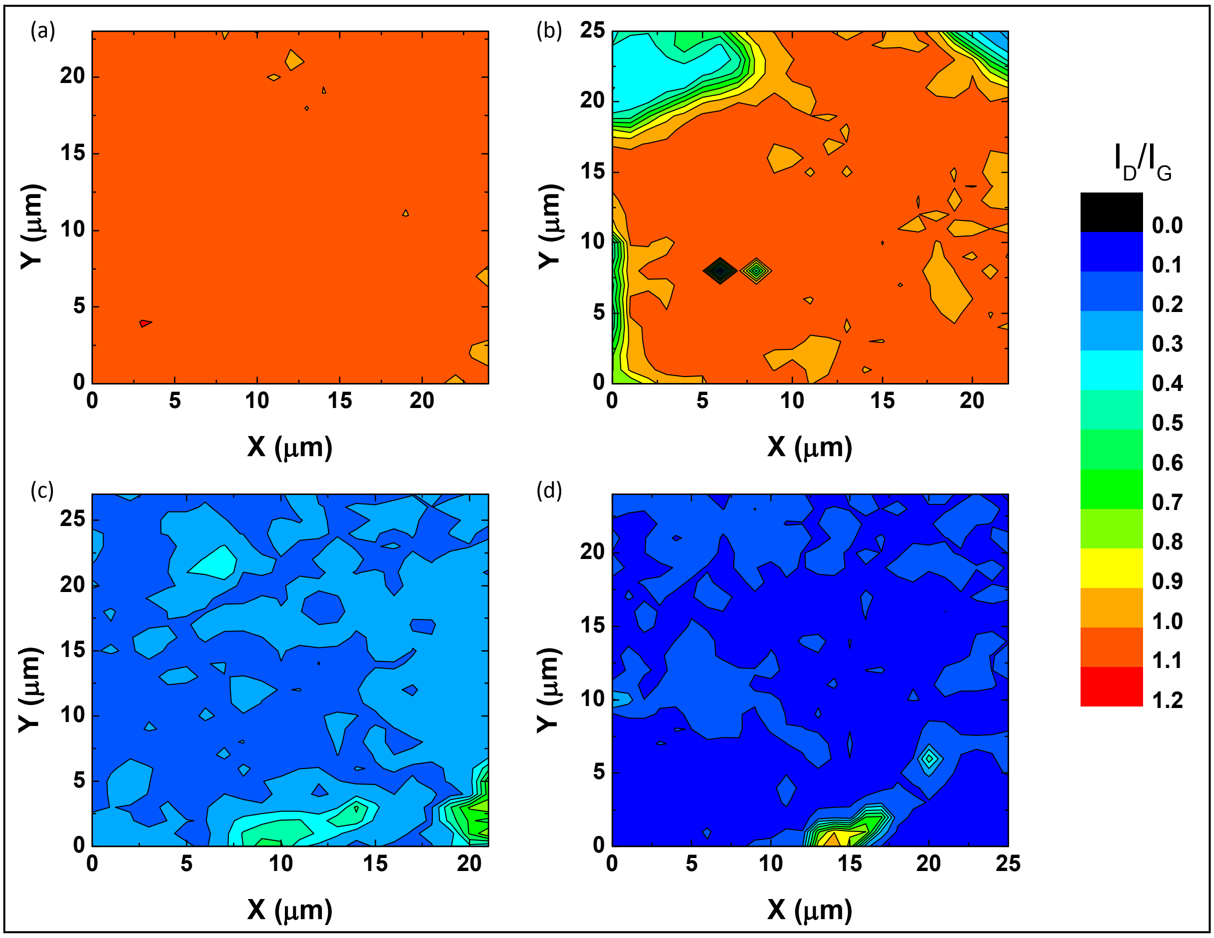

Figure S4. Distribution obtained by Raman spectral imaging of the ordered and disordered areas inside a particle for samples (a) 1, (b) 3, (c) 5 and (d) 7. Colour scale on the right varies with the I_D/I_G values from 0.0 (dark blue) to 1.2 (dark red).

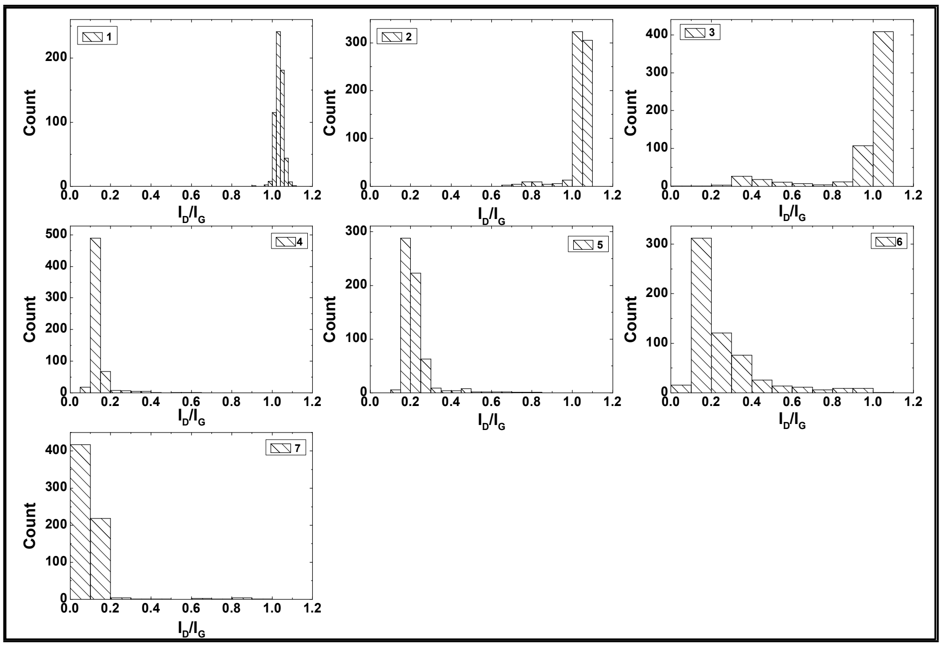

Figure S5. Histogram of each sample calculated from the Raman spectral imaging.

X-Ray diffraction

Figure S6 shows the diffraction profiles for the set of samples studied in the present work. For all the samples a prominent and broad peak at ~ $2\theta = 26°$ corresponding to the (002) diffraction in graphite was clearly evidenced.

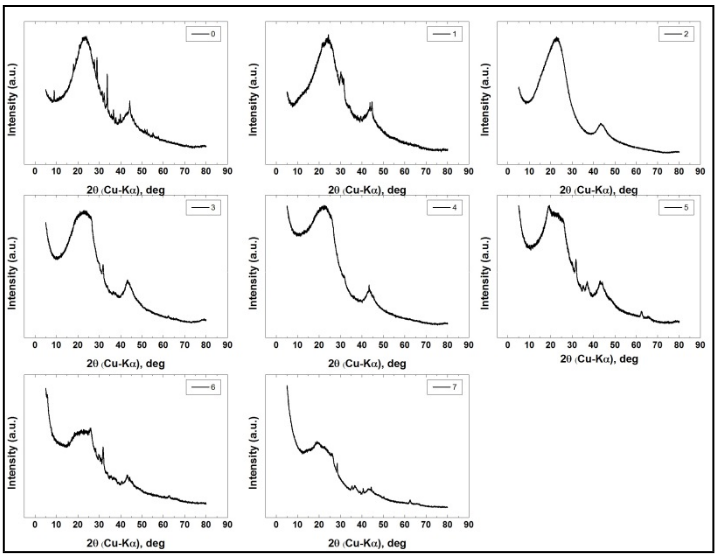

Figure S6. X-Ray diffraction patterns of the lignin-derived carbons.

Electrochemical Characterization

Figure S7 (a) shows the linear dependence of the capacitance on the average micropore size of samples 2 to7 in 1.5 M NEt_4BF_4/ACN. Capacitance values were calculated from galvanostatic charge/discharge curves at 0.1 $A.g^{-1}$ and average micropore size was calculated by 2D-NLDFT method (Table S1). The results show that as the micropore size increases, it becomes more adapted to the ion size and therefore the capacitance values are increased. The average micropore size does not follow a linear tendency with the KOH/C ratio and therefore no trend is observed for the KOH/C ratio or the surface areas (Figure S7(b)) and the capacitance values.

Cyclic voltammograms, performed at a constant scan rate of 5 $mV.s^{-1}$ (Figure S7(c)), evidenced the typical EDLC rectangular shape during the electrosorption of ions for sample 7 and slightly distorted curves for samples 3 and 5. Sample 7 evidenced micropores with a size big enough (0.98 nm) for the adsorption of bare and partially solvated organic ions;[vi] however, samples 3 and 5 have pore sizes much smaller than the solvated ion. These findings suggest that the ion solvation shell becomes highly distorted and partially removed when the ions penetrate into the pores while still enabling an optimum interaction between the ions and the adjacent pore walls.[vii,viii]

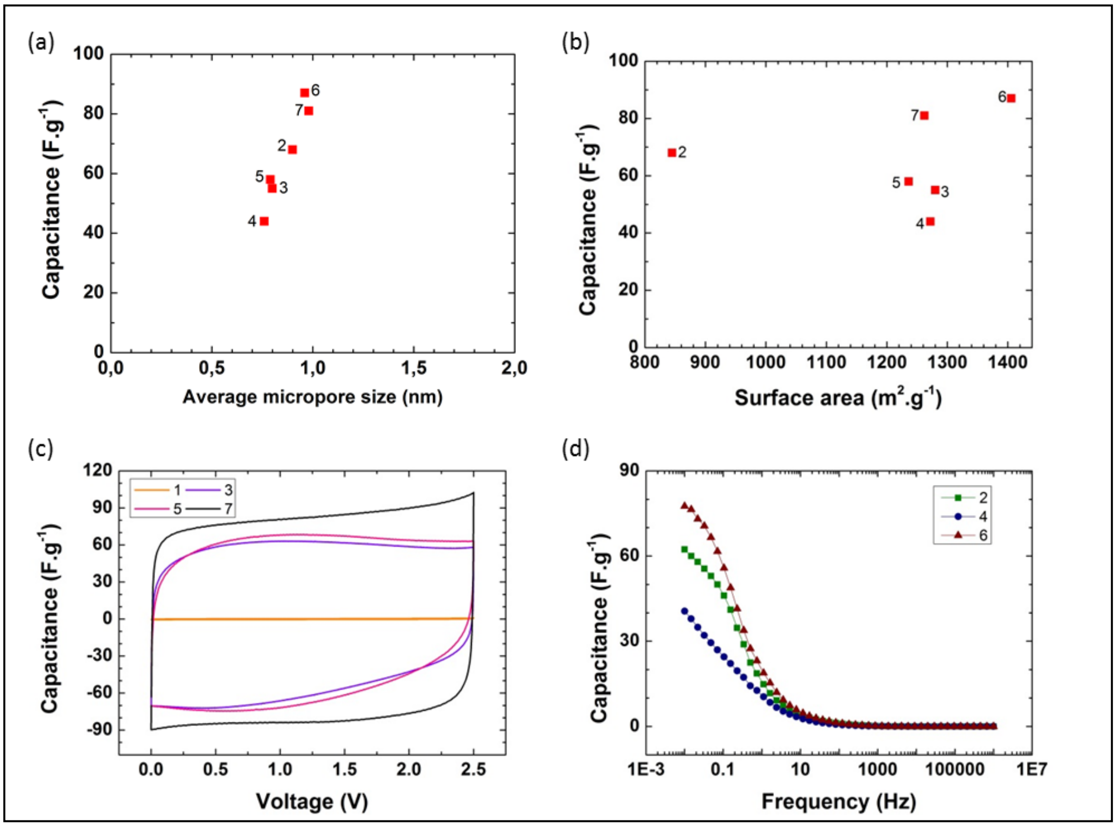

Figure S7. (a) Relationship between gravimetric capacitance and the average micropore size (a) and the specific surface area (m^2/g) (b); the numbers correspond to the name of the samples, (c) CV of samples 1, 3, 5 and 7 in an NEt_4BF_4/ACN and (d) Capacitance versus frequency plots for samples 2, 4 and 6 obtained at OCV.

The specific capacitance value was also determined from EIS data using a series-RC circuit model in which capacitance per electrode is calculated by the following equation[ix]:

$$C_{grav} = \frac{1}{\left|\pi f Z_f'' m\right|} \tag{S2}$$

where f is the frequency, Z_f'' is the imaginary part of the impedance and $\boldsymbol{m}$ is the active mass of the electrode.

Figure S7(d) shows capacitance versus frequency plots obtained for samples 2, 4 and 6 from EIS measurements. At low frequency, the ions can penetrate deeper into the pores resulting in high capacitance values. As the frequency increases the ions stop going further into the pores and access the surface of pore entrances, which leads to a steep decrease on the capacitance. These capacitance values follow the trend observed in the CV curves (Figure 5(a)) achieving the highest gravimetric capacitance values for sample 6 (78 F.g^{-1}) and the lowest for sample 4 (41 F.g^{-1}).

---

[i] T. Shimada, T. Sugai, C. Fantini, M. Souza, L.G. Cançado, A. Jorio, M.A. Pimenta, R. Saito, A. Grüneis, G. Dresselhaus, M.S. Dresselhaus, Y. Ohno, T. Mizutani and H. Shinohara, *Carbon*, 2005, **43**, 1049-1054.

[ii] A. C. Ferrari and J. Robertson, *Phys. Rev. B,* 2000, **61 (20)**, 14095-14107.

[iii] A.C. Ferrari, *Solid State Commun.,* 2007, **143**, 47-57.

[iv] F. Tuinstra and J.L. Koenig, *J. Chem. Phys*., 1970, **53**, 1126-1130.

[v] D. Akbar and Ü.E. Güngör, *Surf. Coat. Technol.*, 2014, **240**, 233-242.

[vi] R. Lin, P.L. Taberna, J. Chmiola, D. Guay, Y. Gogotsi and P. Simon, *J. Electrochem. Soc.*, 2009, **156(1)**, A7-A12.

[vii] C. Largeot, C. Portet, J. Chmiola, P.L. Taberna, Y. Gogotsi and P. Simon, *J. Am. Chem. Soc.*, 2008, **130(9)**, 2730-2731.

[viii] J. Chmiola, C. Largeot, P.L. Taberna, P. Simon and Y. Gogotsi, *Angew. Chem.,* 2008, **120**, 3440-3443.

[ix] R. Kötz and M. Carlen, *Electrochimica Acta*, 2000, **45**, 2483-2498.